Heavily impregnated ceria nanoparticles with europium oxide: spectroscopic evidences for homogenous solid solutions and intrinsic structure of Eu^{3+}-oxygen environments

Daniel Avram · Codruta Rotaru · Bogdan Cojocaru ·
Margarita Sanchez-Dominiguez · Mihaela Florea ·
Carmen Tiseanu

Abstract We report on the homogeneity, structural and luminescence properties of ceria nanoparticles doped with Eu^{3+}. Eu^{3+} in concentration of 1, 5 and 10 wt% was incorporated via wetness impregnation into preformed ceria nanoparticles followed by calcination in air at 1000 °C. A remarkable homogeneity of Eu^{3+}-ceria solid solutions is measured for ceria grown by citrate and micro-emulsion methods using Raman, Diffuse Reflectance in UV–Vis, photoluminescence spectroscopies and X-ray diffraction, even for the Eu^{3+} concentration of 10 wt%. The emission properties of all Eu^{3+}-doped ceria samples are well-characterized by a two main centre model assigned to perturbed and isolated Eu^{3+} centres. These centres correspond to Eu^{3+} located in the nearest (local symmetry lower than cubic and Eu^{3+}-oxygen coordination lower than eight) and next-nearest-neighbour positions (cubic local symmetry and eightfold Eu^{3+}-oxygen coordination) to oxygen vacancy, respectively. With increase of Eu^{3+} concentration, both the oxygen vacancy concentration and the relative contribution of the perturbed Eu^{3+} centre to the total emission increase. It is established that the characteristic emission and excitation spectra of the two main Eu^{3+} centres as well as the overall multisite distribution of Eu^{3+} within ceria lattice are intrinsic properties of Eu^{3+}-doped ceria since these do not depend on synthesis route, nanoparticle size and Eu^{3+} concentration.

Introduction

Ceria (CeO$_2$) doped with trivalent yttrium and lanthanide (Ln^{3+}) ions is extensively investigated due to their elevated oxygen storage capacity (OSC) combined with the ability to shift easily between the redox pair Ce^{4+} and Ce^{3+} oxidation states [1]. Besides its classical use as a catalyst or catalyst support, ceria also presents interest for biomedicine, radical scavenging antioxidants and biological labels applications [2, 3]. The 'marriage' of the europium dopant and ceria host is expected to enhance these applications due to the luminescence properties of Eu^{3+} and also to shed

D. Avram · C. Tiseanu (✉)
National Institute for Laser, Plasma and Radiation Physics,
P.O. Box MG-36, 76900 Bucharest-Magurele, Romania
e-mail: tiseanuc@yahoo.com

D. Avram
e-mail: radu.avram@inflpr.ro

C. Rotaru · B. Cojocaru · M. Florea
Department of Chemical Technology and Catalysis, University
of Bucharest, 4–12 Regina Elisabeta Bvd., Bucharest, Romania
e-mail: rotaru_codruta@yahoo.com

B. Cojocaru
e-mail: bcojocaru@gmail.com

M. Florea
e-mail: mihaela.florea@g.unibuc.ro

M. Sanchez-Dominiguez
Centro de Investigación en Materiales Avanzados,
S. C. (CIMAV), Unidad Monterrey, Alianza Norte 202,
66600 Apodaca, Nuevo León, Mexico
e-mail: margarita.sanchez@cimav.edu.mx

M. Sanchez-Dominiguez
Instituto de Quimica Avanzada de Cataluna, Consejo Superior de
Investigaciones Cientificas (IQAC-CSIC), CIBER en
Biotecnologia, Biomateriales y Nanomedicina (CIBER BBN),
Jordi Girona 18–26, 08034 Barcelona, Spain

light on the local structure properties due to the well-known luminescence sensitivity of Eu^{3+} to nearest ligand (oxygen) environments [4, 5]. To date, literature on Eu^{3+} doped ceria evidences for considerable changes of host and dopant physical properties as a result of the symmetry diversity (cubic to lower symmetries) at Eu^{3+} sites, Eu^{3+} concentration, thermal treatment conditions, Ce^{3+} concentration and so on [2, 6–15]. It is generally considered that the lanthanide dopants with larger ionic radii than Gd^{3+} such as Eu^{3+} repel the oxygen vacancy at the next-nearest-neighbour (NNN) location [1], and thus the Eu^{3+} may preserve the eightfold coordination of O_h symmetry which characterizes the lattice Ce^{4+} sites. However, literature offers strong spectroscopic evidences that besides cubic sites, Eu^{3+} is distributed also on a second site with a non-centrosymmetric, lower symmetry, and its relative contribution to the total emission is increased with concentration or/and calcination temperature. Concerning the nature of this second site, this is not fully elucidated in literature cited above, being attributed to one of the following factors: conversion of 'bulk' to surface Eu^{3+}, interstitial sites, Eu^{3+}-substituted Ce^{4+} associated with defect such as oxygen vacancy or increased covalency of the Eu^{3+}-oxygen bond or combined effect of the excess of oxygen vacancies, increased Ce^{3+}/Ce^{4+} ratio and phase miscibility due to reduction process. Furthermore, issues such as the dependence of the local structure and distribution of Eu^{3+} on ceria lattice sites on the synthesis method, size and concentration are not addressed yet.

Here, we report on homogeneity, structural and luminescence properties of Eu^{3+} doped CeO_2 nanoparticles presented using X- ray Diffraction (XRD), Diffuse Reflectance in UV–Vis (DR–UV/Vis), Raman and photoluminescence spectroscopies. Ceria nanoparticles were synthesised by micro-emulsion and citrate methods or purchased from Aldrich. Eu^{3+} was added, via wetness impregnation, on preformed ceria nanoparticles in concentration of 1, 5 and 10 wt%. The homogeneity of the Eu^{3+}-CeO_2 solid solutions was carefully established using all mentioned above techniques. Next, the characteristic emission and excitation spectra of the main Eu^{3+} centres, their nature and dependencies on the synthesis method, nanoparticle size and Eu^{3+} concentration were determined. To our knowledge, this is the first study aiming at establishing the intrinsic distribution of Eu^{3+} on ceria lattice sites.

Materials and methods

Synthesis

The ceria nanocrystals were obtained using a recently developed micro-emulsion reaction method under soft conditions (ow) [16], citrate method (cit) [17] and commercial

(com, Aldrich, 99.995 % trace metals basis; it was used as received). In our preparation procedure, $Ce(NO_3)_3 \cdot 6H_2O$ was dissolved in 100 mL of distilled water heated at 60 °C and the solution was stirred for 10 min. Citric acid (Merck 244) was added with 10 wt% excess over the stoichiometric quantity for the complete complexation of the metal ions to this solution and the stirring was continued for 1 h at 60 °C. The solution was partially dehydrated in a rotary evaporator at 40 °C until the appearance of a colourless gel. The gel was then dried for 5 h under vacuum at 60 °C and then at 120 °C in air for another 12 h. During this treatment an intense production of nitrogen oxide vapours occurred. A spongy yellowish amorphous solid was obtained.

For the ow preparation, the micro-emulsion system was: water/Synperonic®10/6 (hexaethylene glycol isodecyl ether, technical grade, Croda)/hexane. Cerium (III) 2-ethylhexanoate (Aldrich) was used as organometallic precursor. The composition used was: 64.5 wt% water, 21.5 wt% surfactant and 14 wt% oil phase (hexane solution of Cerium (III) 2-ethylhexanoate). All the components were mixed to obtain an isotropic solution (micro-emulsion) at a temperature of 35 °C. The pH of the solution was then increased to 11 by the addition of concentrated ammonia (25 %, Merk) under vigorous stirring and left for 48 h. The obtained ceria powder was washed using a mixture of ethanol and chloroform (1:1), dried overnight at 70 °C and grinded using an agate pestle and mortar. For the preparation of Eu^{3+} containing samples (1, 5 and 10 wt%), 1 g of dried CeO_2 was impregnated with the required amount of a 0.004 M solution of $EuCl_3 \cdot 6H_2O$ (Fluka). The suspension was stirred 12 h at 60 °C and then water was evaporated at 80 °C. Drying of the samples was continued at 80 °C in vacuum for 4 h. The samples were calcined in air for 4 h at 1000 °C with a heating rate of 5 °C/min.The samples were denoted as CE(ow)-x, CE(cit)-x and CE(com)-x where x refers to Eu^{3+} concentration (1, 5 and 10 wt%).

Characterization

Powder X-ray diffraction (XRD) patterns were recorded on a Schimadzu XRD-7000 diffractometer using Cu Kα radiation ($\lambda = 1.5418$ Å, 40 kV, 40 mA) at a step of 0.2 degrees and a scanning speed of 2 degrees min⁻¹ in the 10°–90° 2Θ range. Crystalline phase was identified by comparasion of the XRD patterns with the JCPDS database. Diffuse reflectance UV–Vis spectra were recorded at room temperature on a Analytik Jena Specord 250 spectrophotometer with an integrating sphere for reflectance measurements and Spectralon as the reflectance standard. DR–UV/Vis spectra of the catalysts were recorded in reflectance units and were transformed in Kubelka–Munk remission function F(R). The differential thermal analysis and thermogravimetric analysis were carried out using a TG–DTA analyser

(Shimadzu DTG-60 Simultaneous DTA-TG Apparatus) in nitrogen atmosphere under the heating rate of 10 °C/min from room temperature to 900 °C and using alumina as reference. Raman analysis was carried out with a Horiba Jobin–Yvon–Labram HR UV–Visible–NIR Raman Microscope Spectrometer, at a laser wavelength of 514 and 488 nm, respectively.

Photoluminescence measurements

The photoluminescence (PL) measurements were carried out using a Fluoromax 4P spectrofluorometer (Horiba) operated in both the fluorescence and the phosphorescence mode. The repetition rate of the xenon flash lamp was 25 Hz, the integration window varied between 300 ms and 3 s, the delay after flash varied between 0.03 and 10 ms, and up to 100 flashes were accumulated per data point. The slits were varied from 0.001 to 10 nm in excitation as well as emission. PL decays were measured using the 'decay by delay' feature of the phosphorescence mode. Time-resolved emission spectra (TRES) were recorded at room temperature using a wavelength tunable NT340 Series EKSPLA OPO (Optical Parametric Oscillator) for samples excitation at 340–360 nm, 457, 488, 460–470 and 514 nm operated at 10 Hz as excitation light source and an intensified CCD camera (Andor Technology) coupled to a spectrograph (Shamrock 303i, Andor) as detection system. The TRES were collected using the box car technique. The initial gate delay (delay after laser pulse, δt) was set to 1 μs and the gate width δt was varied between 10 and 300 μs. The number of accumulations per laser pulse was varied from 50 up to 500. The PL was detected in the spectral range of 500 nm $< z\lambda_{em} < 750$ nm with a spectral resolution of ~ 0.25 nm. All measurements were performed at room temperature (300 K). The PL decays were analysed by fitting with a multiexponential function f(t) using the commercial software (OriginPro 8):

$$f(t) = \sum A_i \exp(-t/\tau_i) + B \tag{1}$$

where A_i is the decay amplitude, B is a constant (the baseline offset) and τ_i is the time constant of the decay i. The average PL lifetime was calculated as amplitude-weighted

$$\tau_A = \frac{\sum\limits_i A_i \tau_i}{\sum\limits_i A_i} \tag{2}$$

Results and discussion

Structural and homogeneity properties

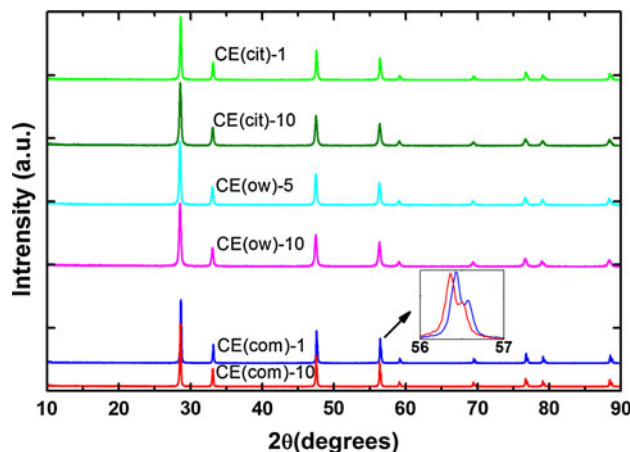Figure 1 presents the X-ray diffractograms of investigated CE samples. In all cases, the diffraction peaks can be

Fig. 1 XRD patterns of Eu^{3+} doped ceria nanoparticles

indexed as a pure cubic fluorite CeO$_2$ structure, which coincide well with the standard data of CeO$_2$ (PDF 00-043-1002). Except for commercial ceria, for which a strong asymmetry was observed around 220 reflection at $\sim 47.5°$, no other phases were observed even for the greatest Eu^{3+} concentration of 10 wt%. With increase of Eu^{3+} amount from 1 to 10 wt%, the crystallite size decreased from 41 to 30 nm in CE(cit) and from 38 to 30 nm in CE(ow) as determined with Debye–Scherrer equation. No significant changes of the particle size were observed for CE(com) samples, with crystallite size varying only slightly from 52 to 55 nm for the similar concentration range of Eu^{3+}. This is most probably due to the thermal pretreatment done by the manufacturer, which prohibits the full incorporation of Eu^{3+} dopants (see also thermo-gravimetric analysis of the undoped ceria samples in Supplemental Information).With the increase of Eu^{3+} concentration, the peak positions of reflections shift to lower 2θ angles which indicates that the doped ceria lattice expands with the increase in dopant content. This result is a consequence of the greater ionic radius of Eu^{3+} compared to Ce^{4+}, in eightfold coordination (1.066 and 0.97 Å), respectively [18].

Overall, the XRD patterns sustain an effective incorporation of Eu^{3+} in the network of ceria for CE(cit) and CE(ow) nanoparticles. The capability of ceria to dissolve lanthanide oxides (in concentration of up to 30 % and using a milder calcinations, of 400 °C) was recently observed by Corma et al. [19]. The property is assigned to nanometric dimensions of ceria since for the micrometric ceria, a similar homogenous distribution of the lanthanide dopant within the lattice was not found.

DR-UV/Vis spectra (Fig. 2) show a strong absorption band below 400 nm which is typical for ceria, assigned to the charge-transfer transition from O^{2-} (2p) to Ce^{4+} (4f) orbitals in CeO$_2$ [20]. It is noteworthy that the Eu^{3+} f–f absorptions are not detected except for the case of
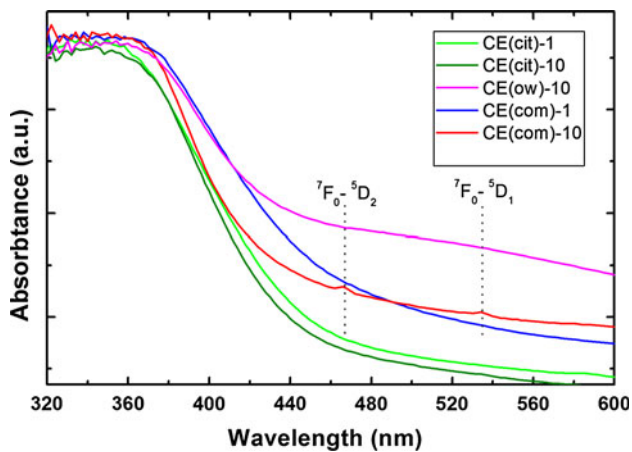
Fig. 2 DR–UV/Vis spectra of selected Eu^{3+} doped ceria nanoparticles

commercial ceria for which peaks at 466 and 535 nm are assignable to Eu $^7F_0$–$^5D_{2, 1}$ absorptions in the Eu_2O_3 oxide.

Next, the formation of homogenous solid solutions and defects is described using Raman spectroscopy. To overcome possible ambiguities in the structural information obtained from Raman spectra, two Vis laser excitation wavelengths at 488 and 514 nm were employed. As recently shown, luminescence bands of lanthanides usually detected outside the phonon range (>800 cm^{-1}) can interfere with phonon bands of ceria based materials, [21] even when present as unintentional impurities (concentration in the ppm range). On the other side, the presence of the luminescent impurities can play a positive role when used as structural probes. Therefore, we analyse the vibrational properties of the ceria host and luminescence of Eu^{3+} from the Raman spectra measured within extended spectral region, namely from 150 to 4000 cm^{-1}, [22, 23].

Figure 3 and Fig. S2 gathers the Raman spectra of Eu^{3+} doped CeO_2 (ow), CeO_2 (com) and CeO_2 (cit), respectively. Irrespective of the sample, the Raman spectra are characterized in the spectral range of phonon bands, by a strong, narrow phonon band around 460–470 cm^{-1} which corresponds to the F_{2g} mode of the CeO_2 fluorite phase along with weaker bands around 250, 600 and 1165 cm^{-1}, due to second-order transverse acoustic (2TA) defect-induced (D) and second-order longitudinal optical (2LO) modes, respectively [24].

Further, the enhancement of the spectral feature around 550 cm^{-1} together with the F_{2g} band shift by ~ 4 cm^{-1} to lower energy is evident for the concentrated samples (ow, cit). The spectral feature at 550 cm^{-1} is assigned to the oxygen vacancies [25] which are generated upon Ce^{4+} substitution by Eu^{3+}. With the increasing Eu^{3+} concentration, the F_{2g} mode becomes asymmetric, broader and slightly shifted to lower wavenumber which is related to the combined effects of strain and phonon confinement resulted
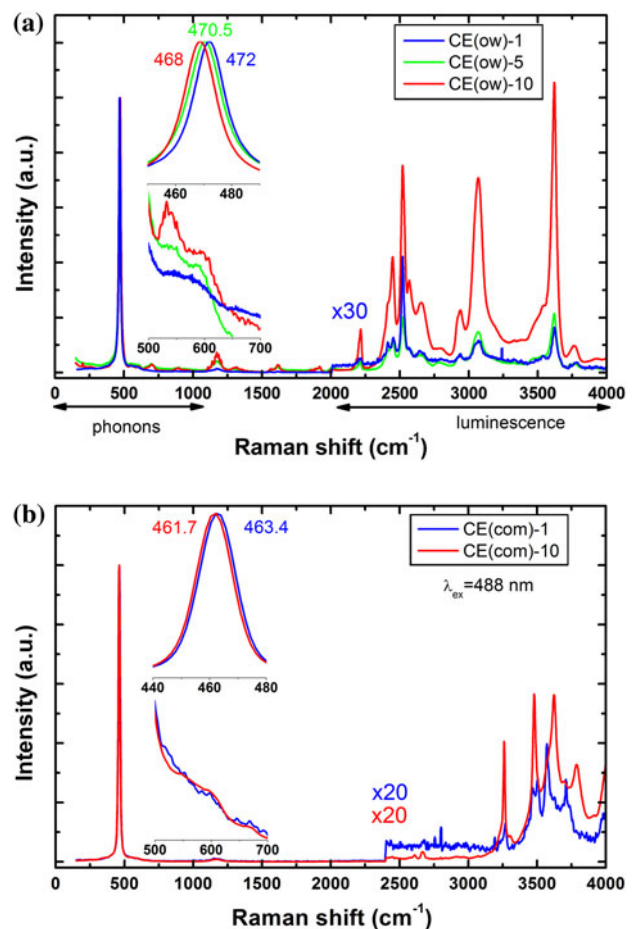

Fig. 3 Raman spectra of Eu^{3+} doped ceria (ow, com) nanoparticles ($\lambda_{ex} = 488$ and 514 nm)

from the decrease of the crystallite size [26, 27]. These observations agree with the XRD results since the crystallite size decreases when increasing the Eu^{3+} content (Fig. 1). Comparative analysis of the Raman spectra of CE(ow) and CE(cit) samples (Fig. S2) measured at 488 and 514 nm did not evidence bands assignable to phonon modes of Eu_2O_3 (such as a feature at 610 cm^{-1}) according to Hernandez et al. [27]. For CE(com) no difference between CE(com)-1 and CE(com)-10 was measured which agrees with limited incorporation of Eu^{3+} in ceria lattice determined previously by XRD and DR–UV/Vis analysis. Instead, very weak bands around 340 cm^{-1} observed at the two excitation wavelengths may be tentatively assigned to the strongest phonon mode (F_g) of Eu_2O_3 cubic phase [28]. Besides the phonon bands of CeO_2, several narrow and relatively intense bands in the spectral range of ~ 1500–4000 cm^{-1} are observed which change strongly with concentration and excitation wavelength. These lines correspond to the electronic luminescence transitions of Eu^{3+} substituting for Ce^{4+} sites in CeO_2 lattice and their detailed description is presented below. It is noteworthy to mention here that the

luminescence of Eu^{3+} in Eu_2O_3 parasite forms is absent in the Raman spectra, since Eu_2O_3 displays strongly different shape and peaks values [29] as those illustrated in Fig. 3 (see also Fig. S2).

Intrinsic structure of Eu^{3+} centres in ceria nanoparticles

Figure 4 illustrates the steady-state emission and excitation spectra of CE(ow)—1, 5, 10 and CE(cit)—10 samples. The emission spectra were excited at two excitation wavelengths, corresponding to the maximum of the charge-transfer absorption band of ceria corresponding to the Ce^{4+}–O^{2-} transition (340–370 nm) and $^7F_0$–$^5D_2$ absorption of Eu^{3+} (around 466 nm). Upon excitation into the CT band, the emission is dominated by the $^5D_0$–$^7F_1$ MD transition at 591 nm which corresponds to Eu^{3+} located in the high symmetry (O_h) sites of ceria lattice. For O_h symmetry, only transitions with $\Delta J = 0, 1$ are allowed (except for $J = 0 \leftrightarrow -J = 0$). Because ionic radius of Eu^{3+} ion is higher than that of Ce^{4+} in eightfold coordination, it is expected that Eu^{3+} interacts with the oxygen vacancy in the next-nearest-neighbour (NNN) position, and the local symmetry at Eu^{3+} sites corresponds to that of Ce^{4+} in cubic fluorite sites [1]. However, the existence of relative strong emission lines in the range of $^5D_0$–$^7F_2$ electric dipole (ED) transition (at 611 and 632 nm) and $^5D_0$–$^7F_0$ (at 580 nm) sustains for multisite distribution of Eu^{3+} in ceria. The relative emission contribution of 611 and 632 nm peaks to the overall emission intensity is enhanced with Eu^{3+} concentration and is changed by shifting the excitation wavelength from ceria CT band to Eu^{3+} f–f absorption at 466 nm. It is acknowledged that the intensities ratio defined as I ($^5D_0$–$^7F_2$)/I ($^5D_0$–$^7F_1$) known as asymmetry ratio, (R) is sensitive to the local asymmetry of the Eu^{3+}-oxygen coordination polyhedron, being higher for low local symmetry at Eu^{3+} sites [30, 31].

The asymmetry ratio increases with the increase of concentration from 0.45 to 1.28 (excitation into CT band) and from 1.5 to 1.9 (excitation at 466 nm) (Fig. 4a, b). Here, R refers to an 'average' local symmetry, as emission spectra are related to a sum of emissions corresponding to cubic (isolated) and low symmetry (perturbed) Eu^{3+} centres. The perturbation is most probably related to short-range interaction between Eu^{3+} and oxygen vacancy located in the nearest-neighbour (NN) site which lowers the symmetry, removes the inversion centre, allowing the observance of the ED transitions. The increase with Eu^{3+} concentration of the relative contribution of the perturbed Eu^{3+} centre to the total emission parallels the increase of oxygen vacancy concentration as established with Raman spectra (see insets in Figs. 3 and S2).

To establish the sensitization pathway of Eu^{3+} emission in the two sites, we compare the steady-state and time-resolved excitation spectra corresponding to the cubic
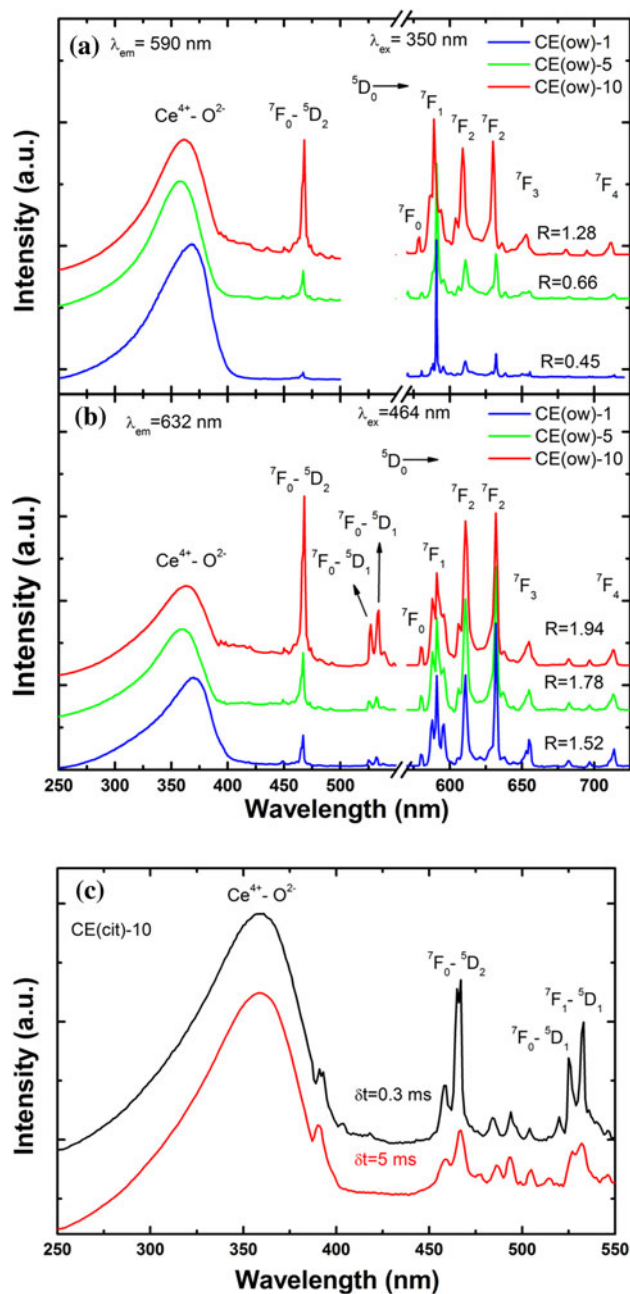

Fig. 4 a, b Steady-state excitation and emission spectra of Eu^{3+} doped ceria (ow) nanoparticles. Excitation, emission wavelengths and values of the asymmetry ratio, R are indicated on the Figure; **c** Time-resolved excitation spectra measured for CE (cit)-10 corresponding to cubic centre emission (591 nm) measured at two different delays after the lamp pulse

centre (emission set at 591 nm) and perturbed centre (emission set at 611 or 632 nm) for the three Eu^{3+} concentrations. Figure 4a, b illustrates the case for Eu^{3+}-CeO_2 (ow) and shows that the cubic centre is excited predominantly via the CT band while the perturbed centre is excited predominantly via the Eu^{3+} f–f absorptions (with that at 466 being the most intense). We should, however,

remark the presence of a non-negligible spectral overlap between the two centre emissions at both wavelengths of 591 and 632 nm. For example, the contribution of the CT band in the excitation of perturbed centre emission might be overestimated since around 632 nm, the emission of the cubic centre, though weak, is non-zero. Conversely, the contribution of the 466 nm absorption in the excitation spectrum of cubic centre emission (at 591 nm) might be also overestimated since around 591 nm, the emission of the perturbed centre is not negligible. Such non-selectivity
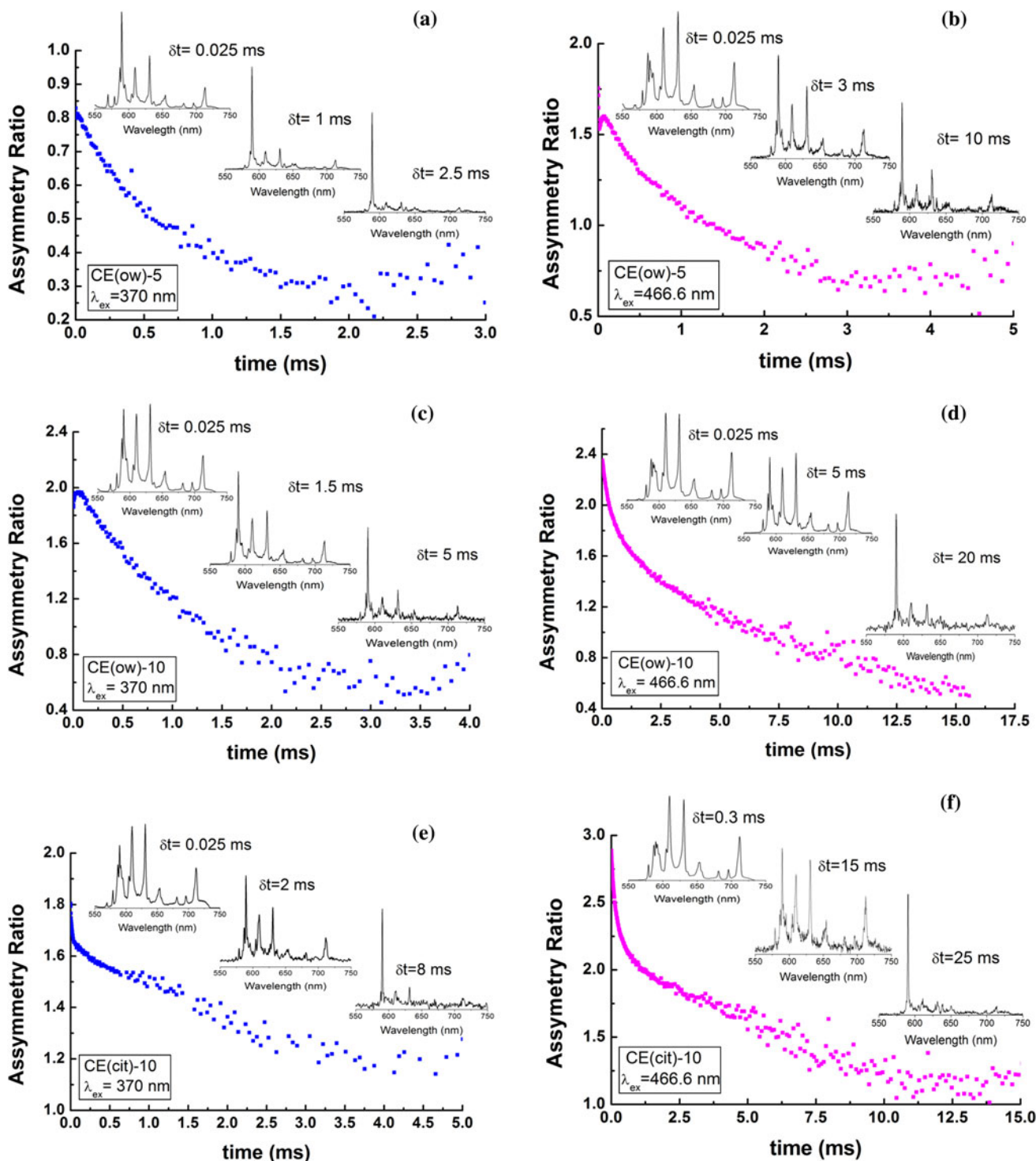

Fig. 5 Evolution with delay after the laser pulse of asymmetry ratio and (peak normalized) emission spectra for CE(ow)-5 (**a, b**), CE(ow)-10 (**c, d**), CE (cit)-10 (**e, f**) upon excitation into CT band (**a, c, e**) and into Eu^{3+} f–f absorption at $\lambda_{ex} = 466.6$ nm (**b, d, f**)

effects are confirmed by the time-resolved excitation spectra (at 591 nm) measured at two different delays, δt, after the lamp pulse and exemplified in Fig. 4c with CE(cit)-10. At a shorter delay (0.03 ms) both emissions are present whereas imposing a longer delay of 5 ms, only the emission of the longer-lived cubic centre is detected. In the latter case, the excitation spectrum contains basically the CT band absorption followed by much weaker f–f absorptions. Nevertheless, despite the difficulty in spectral separation of the two emissions, we can conclude that the perturbed centre is preferentially excited via—f–f absorption at 466 nm whereas the cubic centre is preferentially sensitized via the charge-transfer absorption band of CeO_2.

Figure 5 illustrate the temporal evolution of the (peak normalized) PL spectra of Eu^{3+}-CeO_2 (ow; cit) excited into the CT band and at 466 nm and collected at three delays after the laser pulse. Also included in Fig. 5 is the temporal evolution of the asymmetry ratios for delay increasing from
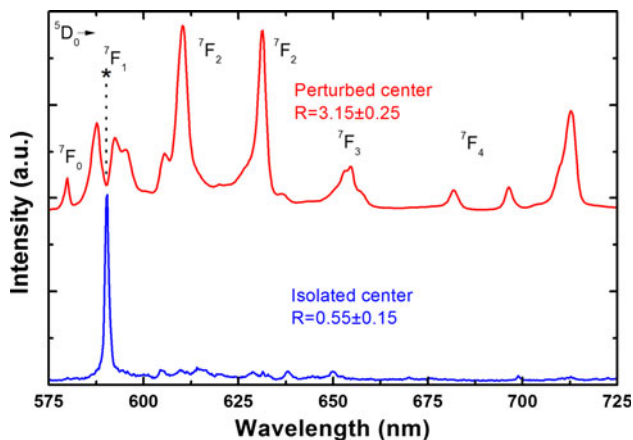

Fig. 6 Fingerprint emission spectra of Eu^{3+} cubic (isolated) and main perturbed centres in Eu^{3+} doped ceria nanoparticles

few μs up to 17.5 ms. For each case, the longest delay was limited by the signal-to-noise ratio. As a general trend, the temporal evolution sustains the superposition of two main emissions with strongly different shapes and decay times. At short delays, the emissions of both Eu^{3+} centres are measured. The emission of the low symmetry centre prevails for the concentrated sample (10 wt%) up to 2 ms after the laser pulse for excitation into CT band and up to 5 ms for excitation at 466.6 nm, whereas the emission characteristic of the cubic centre dominates the emission of the diluted sample when excited into the CT band. Such trends agree with the steady-state emission and excitation spectra illustrated in Fig. 4. At long delays, the emission of the perturbed centre is quenched, and the emission corresponds largely to the cubic Eu^{3+} centre. The 'true' emission spectrum of the cubic centre is extracted from the delayed PL spectra measured at delay times which typically exceed 10–20 ms and by use of up to 500 accumulations per laser pulse. It is noteworthy to mention that the obtained delayed emission spectra are highly similar, irrespective of sample type (see also Fig. S3) and Eu^{3+} concentration.

These findings demonstrate that the local oxygen environments at Eu^{3+} cubic sites in ceria do not depend on synthesis, size and dopant concentration. Furthermore, supposing that the overall emission is given by these two non-interacting centres, we can approximate the emission spectrum of the low symmetry centre as the difference spectrum between the total and cubic related emission spectra, respectively. The difference spectra were obtained both from steady-state emission spectra measured at different concentrations or from time-resolved PL spectra measured at several pairs of delays. The characteristic emission spectra related to the cubic and perturbed Eu^{3+} centres are gathered in Fig. 6. The emission spectrum of the cubic centre (determined experimentally from the
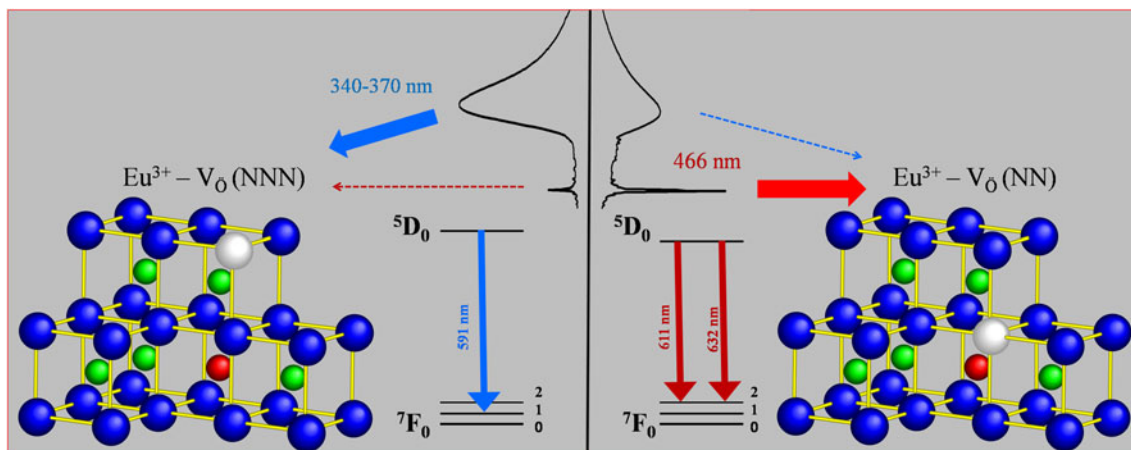
Scheme 1 Two centre model in Eu^{3+} doped ceria nanoparticles. These centres correspond to Eu^{3+} located in the nearest (local symmetry lower than cubic and Eu^{3+}-oxygen coordination lower than eight) and next-nearest-neighbour positions (cubic local symmetry and eightfold Eu^{3+}-oxygen coordination) to oxygen vacancy, respectively
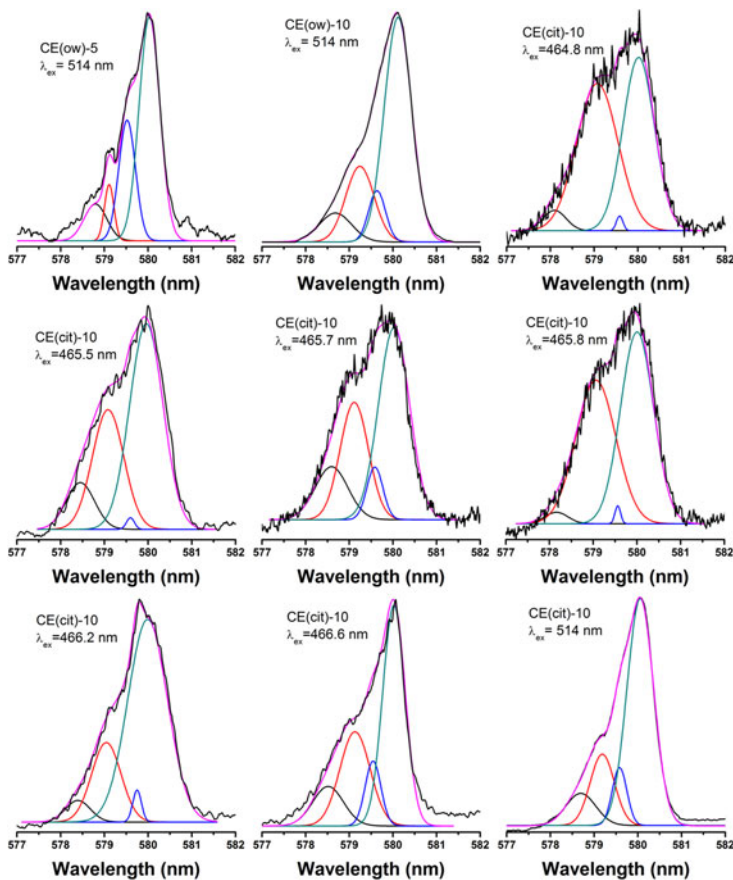
	Peak 1	Peak 2	Peak 3	Peak 4
CE(ow) - 5 λ_{ex}= 514 nm	578.7 nm	579.1 nm	579.5 nm	580 nm
CE(ow) - 10 λ_{ex}= 514 nm	578.6 nm	579.1 nm	579.6 nm	580 nm
CE(cit) - 10 λ_{ex}= 464.8 nm	578 nm	579 nm	579.6 nm	580.1 nm
CE(cit) - 10 λ_{ex}= 465.5 nm	578.4 nm	579.1 nm	579.5 nm	580 nm
CE(cit) - 10 λ_{ex}= 465.7 nm	578.6 nm	579.1 nm	579.5 nm	579.9 nm
CE(cit) - 10 λ_{ex}= 465.8 nm	578.1 nm	579 nm	579.5 nm	580 nm
CE(cit) - 10 λ_{ex}= 466.2 nm	578.3 nm	579 nm	579.75 nm	580 nm
CE(cit) - 10 λ_{ex}= 466.6 nm	578.6 nm	579.1 nm	579.5 nm	580 nm
CE(cit) - 10 λ_{ex}= 514 nm	578.7 nm	579.2 nm	579.6 nm	580 nm

Fig. 7 Lineshape analysis of $^5D_0$–$^7F_0$ emission in Eu^{3+} doped ceria (ow, cit) nanoparticles by use of selective laser excitation; Table 1 (Right) Results of peak deconvolution of $^5D_0$–$^7F_0$ emission

delayed emission spectra) is dominated by the emission at 591 nm with small peaks in the spectral region of the forbidden ED transitions (600–640 nm) and has an asymmetry ratio of 0.55 ± 0.15. The emission spectrum of the perturbed centre is dominated by relatively strong ED emission at 611 and 632 nm, followed by several lines around $^5D_0$–$^7F_1$ and $^5D_0$–$^7F_0$ emissions around 591 and 580 nm, respectively. The asymmetry ratio, R, of 3.15 ± 0.25 confirms a low symmetry around Eu^{3+} centres, which is most probably defined by a short-range interaction between Eu^{3+} and nearest-neighbour (NN) oxygen vacancies [23]. However, the R value is slightly overestimated since the emission of the perturbed Eu^{3+} centre at 591 nm is discarded in the difference spectra (effect marked with '*' on Fig. 6).

Though the co-existence of two main Eu^{3+} centres is consistent with the emission data described here (see also Scheme 1), the actual picture of Eu^{3+} interactions with ceria host is more complex. To demonstrate this, we have performed a close examination of $^5D_0$–$^7F_0$ emission. Since both $^5D_0$ and $^7F_0$ levels are non-degenerate and cannot be split by

the crystal-field, the line shape is informative for the number of different Eu^{3+} crystal-field environments or centres.

Figure 7 gathers the lineshape analysis of $^5D_0$–$^7F_0$ emission in CE(ow) and CE(cit) nanoparticles by the use of selective laser excitation (λ_{ex} = 464.8, 465.5, 465.7, 465.8, 466.2, 466.6 and 514 nm). With change of the excitation wavelength, the shape, peak position (peaks at 578.44 $\pm$ 0.4; 579.08 $\pm$ 0.1; 579.56 $\pm$ 0.2; 580 $\pm$ 0.1 nm) and width of this emission change reflecting the co-existence of minimum four perturbed centres in agreement with the low-temperature data reported earlier [32].

We have also measured PL decays of CE(ow), CE(cit) and CE(com) measured on different emission wavelengths, such as λ_{em} = 580, 591, 611, 632 and 713 nm corresponding to $^5D_0$–$^7F_0$, $^5D_0$–$^7F_1$, $^5D_0$–$^7F_2$, $^5D_0$–$^7F_2$ and $^5D_0$–$^7F_4$ transitions, respectively, with excitations into CT band and at 466 nm. To reveal the main dependencies of PL decays on concentration, emission or excitation wavelengths, selected curves are represented in Fig. 8. As a general feature, all PL decays are non-exponential, irrespective of the sample and excitation or/and emission
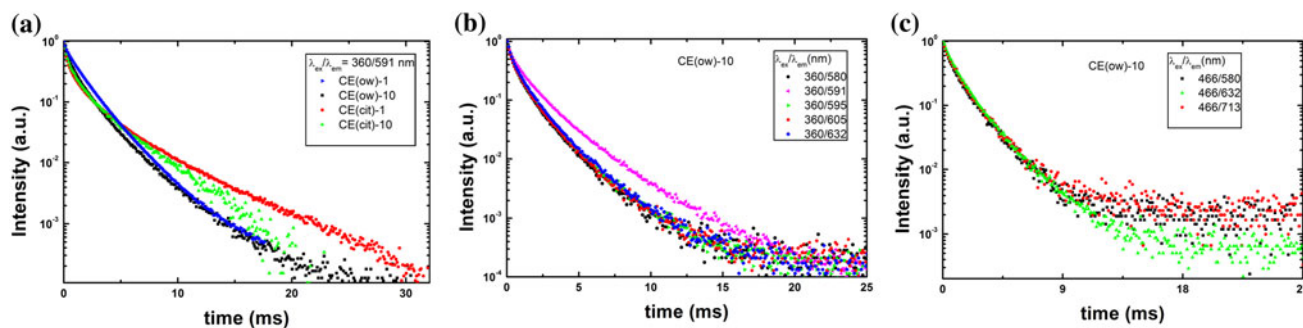
Fig. 8 a Comparison between the PL decays of CE(cit) and CE(ow). Excitation was performed into the CT band and emission was measured around 591 nm (corresponding mainly to emission of the cubic Eu^{3+} centre); **b** Dependence of the PL decays of CE(ow)-10 on emission wavelength. Excitation was performed into the CT band and emission was measured around 580, 591, 595 and 632 nm; **c** Comparison between the PL decays of CE(ow)-10. Excitation was done at 466 nm, and emission was corresponding to the emission of perturbed Eu^{3+} centre

wavelength which is expected given the multicentre structure of Eu^{3+} in ceria samples with strongly overlapped excitation and emission spectra.

Figure 8a gathers the PL decays of CE samples for excitation into the CT band and emission fixed at 591 nm. Such excitation and emission conditions favour the emission of the cubic Eu^{3+} centre. It is noteworthy to remark the absence of a notable emission quenching with Eu^{3+} concentration with the average PL lifetimes (Eq. 2) varying between 0.9 and 1.2 ms. Figure 8b compares the PL decays corresponding to emission of perturbed and cubic Eu^{3+} centres in CE(ow)-10 with excitation into the CT band. The PL decay of the cubic centre (emission wavelength fixed at 591 nm) is generally longer compared to perturbed centre (emission fixed at 580, 595 and 632 nm) which is related to the different radiative transition probabilities of the main emissions. Finally, Fig. 8c gathers the PL decays of the perturbed Eu^{3+} centres (emission wavelength set at 580, 632 and 713 nm) with excitation at 466 nm.

The results evidence also the predominant contribution of the main low symmetry Eu^{3+} centre despite that the co-existence of several minor low symmetry centres is clearly revealed from site selective excited emission spectra (Fig. 7).

Conclusions

Ceria doped with Eu^{3+} obtained by micro-emulsion or citrate methods or purchased were investigated using X-ray Diffraction, DR–UV/Vis, steady-state and time-resolved photoluminescence and Raman spectroscopies. Eu^{3+} was added via wetness impregnation on the preformed ceria nanoparticles in concentration of 1, 5 and 10 wt%, and the obtained samples were calcined in air at 1000 °C. Except for the commercial ceria, a remarkable homogeneity of Eu^{3+}-ceria solid solutions was measured, even for the greatest Eu^{3+} concentration of 10 wt%. Overall emission properties agreed with a intrinsic structure composed of one cubic centre and four low symmetry centres (one main, three minor). It was also established from the emission decays that the concentration quenching was not significant for the isolated Eu^{3+} centres.

References

1. Gerhardt-Anderson R, Nowick AS (1981) Ionic conductivity of CeO$_2$ with trivalent dopants of different ionic radii. Solid State Ionics 5:547–550
2. Kumar A, Babu S, Karakoti AS, Schulte A, Seal S (2009) Luminescence properties of europium-doped cerium oxide nanoparticles: role of vacancy and oxidation states. Langmuir 25:10998–11007
3. Sahu T, Singh Bisht S, Ranjan Das K, Kerkar S (2013) Nanoceria: synthesis and biomedical applications. Curr Nanosci 9:588–593
4. Yan CH, Sun LD, Liao CS, Zhang YX, Lu YQ, Huang HS, Lu SZ (2003) Eu^{3+} ion as fluorescent probe for detecting the surface effect in nanocrystals. Appl Phys Lett 82:3511–3513
5. Reisfeld R, Zigansky E, Gaft M (2004) Europium probe for estimation of site symmetry in glass films, glasses and crystals. Mol Phys 102:1319–1330
6. Fujihara S, Oikawa M (2004) Structure and luminescent properties of CeO$_2$: rare earth (RE = Eu^{3+} and Sm^{3+}) thin films. J Appl Phys 95:12
7. Choudhury B, Choudhury A (2012) Lattice distortion and corresponding changes in optical properties of CeO$_2$ nanoparticles on Nd doping. Curr Appl Phys 13:217–223
8. Liu X, Chen S, Wang S (2007) Synthesis and photoluminescence of CeoO$_2$:Eu^{3+} phosphor powders. J Lumin 127:650–654
9. Wang Z, Quan Z, Lin J (2007) Remarkable changes in the optical properties of CeO$_2$ nanocrystals induced by lanthanide ions doping. Inorg Chem 46:5237–5242
10. Babu S, Schulte A, Seal S (2008) Defects and simmetry influence on visible emission of Eu doped nanoceria. Appl Phys Lett 92:123112

11. Li L, Yang K, Moon BK, Fu Z, Guo C, Jeong JH, Yi SS, Jang K, Lee HS (2009) Photoluminescence properties of $CeO_2:Eu^{3+}$ nanoparticles synthesized by a sol–gel method. J Phys Chem 113:610–617

12. Zeng L, Chen D, Cui L, Huang F, Wang Y (2010) High-content bulk doping and thermal stability of rare earth ions in CeO_2 nanocrystals. Scipta Materialia 63:661–664

13. Tiseanu C, Parvulescu VI, Boutonnet M, Cojocaru B, Primus PA, Teodorescu CM, Solans C, Sanchez-Dominguez M (2011) Surface versus volume effects in luminescent ceria nanocrystals synthesized by an oil-in-water micro- emulsion method. Phys Chem Chem Phys 13:17135–17145

14. Tiseanu C, Parvulescu VI, Sanchez-Dominguez M, Boutonnet M (2012) Temperature induced conversion from surface to "bulk" sites in Eu^{3+}- impregnated CeO_2. J Appl Phys 112:013521

15. Chae KW, Park TR, Cheon CI, Cho NI, Kim JS (2013) Enhanced phasemiscibility and luminescence by inducing oxygen vacancies in $Ce_{1-x}Eu_xO_2$- under a strongly reducing atmosphere. J Lumin 136:109–116

16. Sanchez-Dominguez M, Boutonnet M, Solans C (2009) A novel approach to metal and metal oxide nanoparticle synthesis: the oil-in-water micro- emulsion reaction method. J Nanopart Res 11:1823–1829

17. Courty P, Ajot H, Marcilly C, Delmon B (1973) Oxydes mixtes ou en solution solide sous forme très divisée obtenus par décomposition thermique de précurseurs amorphes. Powder Technol 7:21–38

18. Shannon RD (1976) Revised effective ionic radii and systematic studies of interatomic distances in Halides and Chaleogenides. Acta Cryst 32:751–767

19. Corma A, Atienzar P, Garcia H, Chane-Ching JY (2004) Hierarchically mesostructured doped CeO_2 with potential for solar-cell use. Nat Mater 3:394–397

20. Bensalem A, Muller JC, Bozon-Verduraz F (1992) Faraday communications. From bulk CeO_2 to supported cerium–oxygen clusters: a diffuse reflectance approach, J. Chem Soc, Faraday Trans. 88:153–154. doi:10.1039/FT9928800153

21. Fornasiero P, Speghini A, Di Monte R, Bettinelli M, Kašpar J, Bigotto A, Sergo V, Graziani M (2004) Laser-excited luminescence of trivalent lanthanide impurities and local structure in CeO_2–ZrO_2 mixed oxides. Chem Mater 16:1938–1944

22. Tiseanu C, Cojocaru B, Parvulescu V, Sanchez-Dominguez M, Primus PA, Boutonnet M (2012) Order and disorder effects in nano-ZrO_2 investigated by micro-Raman and spectrally and temporarily resolved photoluminescence. Phys Chem Chem Phys 14(37):12970–12981. doi:10.1039/c2cp41946g

23. Tiseanu C, Parvulescu V, Cojocaru B, Pemartin K, Sanchez-Dominguez M, Boutonnet M (2012) In situ Raman and time-resolved luminescence investigation of local structure of ZrO_2 in the amorphous to crystalline phase transition. J Phys Chem C 116:16776–16783

24. Spanier JE, Robinson RD, Zhang F, Chan SW, Herman IP (2001) Size-dependent properties of CeO_{2-y} nanoparticles as studied by Raman scattering. Phys Rev B 64:245407

25. McBride JR, Hass KC, Poindexter BD, Weber WH (1994) Raman and x-ray studies of $Ce_{(1-x)} RE_{(x)} O_{(2-y)}$, where RE = La, Pr, Nd, Eu, Gd, and Tb. J Appl Phys 76:2435–2441

26. Zhang F, Chan S-W, Spanier JE, Apak E, Jin Q, Robinson RD, Herman IP (2002) Cerium oxide nanoparticles: size-selective formation and structure analysis. Appl Phys Lett 80:127–129

27. Hernandez WY, Centeno MA, Romero-Sarria F, Odriozola JA (2009) Synthesis and characterization of $Ce_{1-x}Eu_xO_{2-x/2}$ mixed oxides and their catalytic activities for CO oxidation. J Phys Chem C 113:5629–5635

28. Dilawar N, Mehrotra S, Varandani D, Kumaraswamy BV, Haldar SK, Bandyopadhyay AK (2008) A Raman spectroscopic study of C-type rare earth sesquioxides. Mat Characterization 59:462–467

29. Eilers H, Tissue BM (1996) Laser spectroscopy of nanocrystalline Eu_2O_3 and $Eu^{3+}:Y_2O_3$ Chem. Phys. Lett. 251:74–78

30. Görller-Walrand C, Fluyt L, Ceulemans A, Carnall WT (1991) Magnetic dipole transitions as standards for Judd–Ofelt parameterization in lanthanide spectra. J Chem Phys 95:3099–3106

31. Oomen EWJL, Van Dongen AMA (1989) Europium (III) in oxide glasses: dependence of the emission spectrum upon glass composition. J Non-Cryst Solids 111:205–213

32. Tiseanu C, Parvulescu V, Sanchez Dominguez M, Boutonnet M (2012) Temperature induced conversion from surface to bulk sites in Eu^{3+}- impregnated CeO_2. J Appl Phys 112:013521